

Nanosecond Radio-Frequency Pulse Driven Photogun for Very Hard X-ray Free-electron Laser

Wei Hou Tan,* River R. Robles, Juan E. Hernandez Jr., Emilio Alessandro Nanni, and Ankur Dhar†
SLAC National Accelerator Laboratory, 2575 Sand Hill Rd, Menlo Park, California 94025, USA

(Dated: November 12, 2025)

One pathway to producing high brightness electron beams is to use a radio-frequency (rf) driven high field photogun to rapidly accelerate photoemitted electrons to the relativistic regime and preserve the brightness. However, the highest attainable field is limited by rf breakdowns of materials used in a photogun. Shortening rf pulse duration feeding into a photogun provides a viable pathway to achieve high field and prevent rf breakdowns. Here we propose and investigate the Compressed Ultrashort Pulse Injector Demonstrator (CUPID), a nanosecond rf pulse driven photogun powered by a klystron and rf pulse compression system capable of achieving 300 MW at 20 ns duration, to produce bright electron beams with high electric field. We first introduce the design of the CUPID photogun and its expected rf performance at 500 MV/m driven by high power nanosecond rf pulses, followed by beam dynamics studies showing its capability for producing bright electron beams with 60 nm emittance when forming a photoinjector with a superconducting solenoid and downstream accelerating structures. Finally, we show a proof-of-concept start-to-end simulation of the CUPID photoinjector paired with the existing Linac Coherent Light Source (LCLS) copper accelerator free-electron laser (FEL) to demonstrate achievable mJ pulse energy very hard x-ray photons at 40 keV or higher.

I. INTRODUCTION

High brightness photoguns have a wide range of scientific applications based on electron accelerators, such as free-electron lasers (FEL) [1]. The launch of the world's first hard x-ray FEL at the Linac Coherent Light Source (LCLS) of SLAC National Accelerator Laboratory opened a new frontier of photon science and found numerous applications in a wide range of research disciplines, such as biology, chemistry and material sciences [2, 3]. These scientific breakthroughs in turn drive the development of x-ray FELs to push for even higher photon and pulse energies, such as x-ray photons at 40 keV or higher, to enable newer scientific studie[s] [4–9].

The performance of a FEL is proportional to the brightness of electron beams, as shown in the relation

$$\rho \propto \mathcal{B}_{6D} = \frac{2I}{\varepsilon_n^2 \sigma_\gamma}, \quad (1)$$

where ρ is the Pierce parameter that characterizes the efficiency of a FEL and \mathcal{B}_{6D} is the six-dimensional beam brightness, I is the beam current, ε_n is the beam normalized transverse emittance and σ_γ is the normalized rms energy spread in terms of the Lorentz factor respectively [1, 10]. In the past, more efforts were often devoted to minimizing the beam's transverse emittance than minimizing the energy spread. The rationale was that transverse emittance was much harder to achieve for FEL requirements, whereas the energy spread was smaller than necessary to suppress instability. For example, LCLS has a device called a laser heater to deliberately

increase the beam's energy spread to suppress shot-noise-induced instability [11]. Hence, one often has to minimize the beam's transverse emittance to improve the beam's brightness. Lower emittance beams allow FELs to output higher x-ray photon energy and increase total pulse energy. Figure 1 shows total pulse energy versus x-ray photon energy for 100 pC 3.5 kA beam at 8 GeV and 15 GeV with transverse emittances from 100 nm to 500 nm, calculated using Ming-Xie parameterization [12]. Beam parameters taken from Fig. 1-3 of ref [1].

The beam brightness is directly influenced by the strength of the applied electric field in a photogun, where a radiofrequency (rf) driven photogun is usually employed to accelerate photoemitted electron beams to high energies to suppress the degradation caused by charge repulsion [13, 14]. The relation of beam brightness and the gradient of applied field is given by $\mathcal{B}_{6D} \propto E^\nu$, where ν is a parameter that depends on the beam shape. For example, for beams with small transverse-to-longitudinal aspect ratio, $\mathcal{B}_{6D} \propto E^2$ [10, 15–18].

However, the use of high gradient electric fields causes rf breakdowns, where uncontrolled field emission of electrons from the inner surface of the gun occurs in large quantities and prevents the build-up of accelerating fields inside the gun [19–22]. Accordingly, the phenomenological model of the breakdown rate is proportional to the applied field gradient but inversely proportional to the rf pulse duration [23]. Increasing the operating frequency allows shorter rf pulse duration, as proposed in various photogun designs at higher frequencies [24–29]. This presents the possibility of achieving a high gradient photogun fed by ultrashort high power rf pulses. This approach was recently demonstrated at the Argonne Wakefield Accelerator (AWA), where an X-band 11.7 GHz gun was operated at ~ 400 MV/m without significant breakdowns [30]. AWA achieved this by using a wakefield ac-

* whtan@slac.stanford.edu

† adhar@slac.stanford.edu

celerator that accelerates 400 nC electron bunches to high energies and generates ~ 9 ns high power rf pulses from a power-extraction-and-transfer structure (PETS) [31]. However, this approach requires a larger physical footprint and additional stability control to operate a dedicated wakefield accelerator.

Here we present Compressed Ultrashort Pulse Injector Demonstrator (CUPID), a 1.6 cell photogun that can achieve high gradient with ultrashort high power rf pulses generated by a novel ultra-high power rf pulse compressor instead of the wakefield accelerator approach of AWA. This photogun operates at 11.424 GHz to utilize an available X-band klystron of the same frequency and rf pulse compressor recently commissioned at SLAC [32].

This paper reports our design work on CUPID for generating bright electron beams that can drive very hard x-rays at the LCLS FEL. We first introduce the design of the CUPID photogun capable of achieving 500 MV/m on cathode with nanoseconds long rf pulses from an existing klystron and recently commissioned rf pulse compressor, operating at 11.424 GHz. We present the rf and mechanical design of the CUPID photogun and its performance. After that, we show the beam dynamics studies of the CUPID photoinjector, where the photogun is paired with a dedicated solenoid, followed by downstream accelerating structures, to demonstrate its capability in generating bright electron beams, down to 60 nm transverse emittance. We then demonstrate start-to-end simulations of the CUPID photoinjector with the existing LCLS copper accelerator to show achievable mJ pulse energy up to 60 keV x-ray.

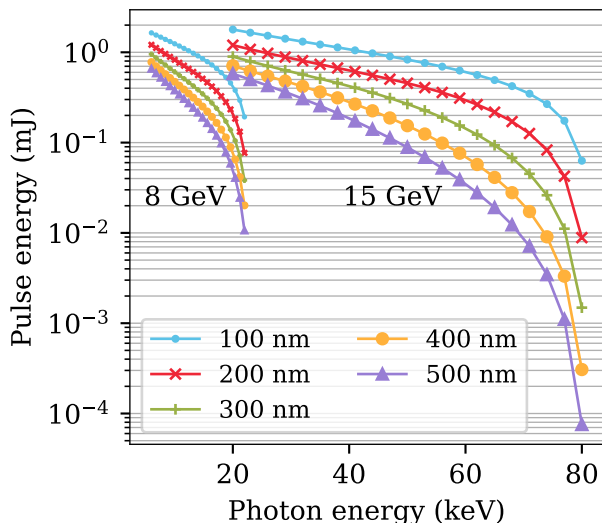


Figure 1. X-ray FEL outputs for different photon energies with 8 GeV and 15 GeV 100 pC 3.5 kA beams with emittances at 100, 200, 300, 400 and 500 nm respectively, calculated using Ming-Xie parameterization. Parameters taken from Fig. 1-3 of ref [1].

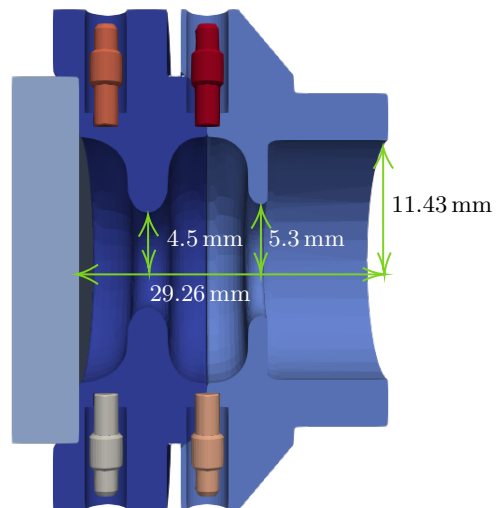


Figure 2. Cut-away view of a solid model of the CUPID photogun. Copper parts are shown in varying shades of blue. The exit of the photogun (right) is designed as a 11.43 mm radius waveguide to connect to a TM_{01} mode launcher. Four tuning pins are available for frequency tuning of both cells. The copper backplate (left) of the photogun serves as the cathode. It has large aperture sizes to reach a very low Q_l .

II. CUPID PHOTOGUN RF DESIGN

A. Design

The CUPID photogun is a 1.6 cell photogun that has a very fast filling time (~ 20 ns) to attain very high gradient electric field with a very short time duration to suppress rf breakdowns. This is achieved by designing the CUPID photogun to be over-coupled to have a very low loaded quality factor,

$$Q_l = \pi f t_{\text{fill}}, \quad (2)$$

where Q_l is the loaded quality factor, f is the frequency, t_{fill} is the rf filling time. For an operating frequency $f = 11.424$ GHz and an input 20 ns pulse that has 7 ns rising time, Q_l needs to be smaller than 251 to have a shorter filling time than the rising time period.

Figure 2 shows a cut-away view of the CUPID photogun design. The exit of the photogun is designed as a 11.43 mm radius waveguide to connect to a TM_{01} mode launcher. A photo of a fabricated prototype cavity being used for upcoming high power tests is also shown in Fig. 3. Four tuning pins are available for frequency tuning of both cells. The cathode for the CUPID photogun is a copper backplate. It has large aperture sizes to reach a very low Q_l .

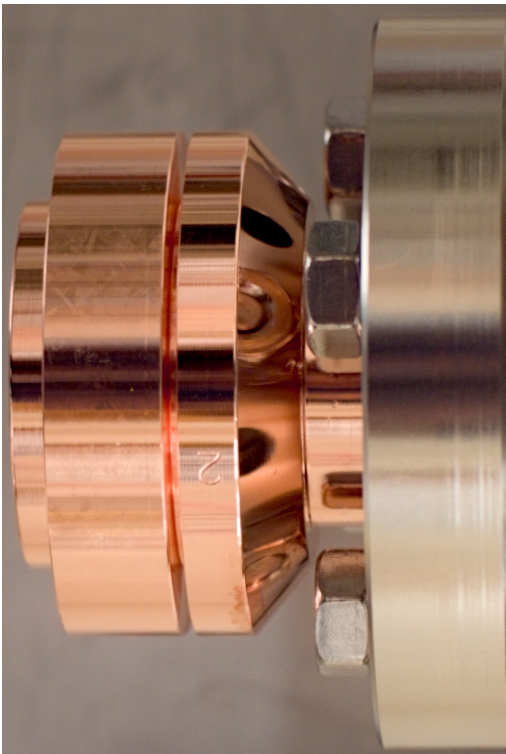


Figure 3. Photograph of fabricated test cavity for CUPID. This cavity will be used in upcoming high power tests to verify the ability to generate high electric fields with short pulses and low breakdown rate.

B. Rf Performance

The electric field gradient at the cathode is designed to operate at 500 MV/m fed by high power nanosecond rf pulses. This is achieved by using rf pulse compressors in conjunction with a high power klystron rf source. The 500 MV/m gradient is chosen to match the normalized field strength parameter $\alpha_{\text{rf}} = eE\lambda/4\pi mc^2 \approx 2$ of the LCLS S-band 120 MV/m photogun [15, 33]. For initial tests, the CUPID photogun is planned to connect to the available TM_{01} X-band mode launcher [34, 35]. Figure 4 shows the cut-away view of the CUPID photogun, the connecting waveguide and the TM_{01} mode launcher, with the π -mode field map. The relatively long waveguide connecting both components is a design choice to

Table I. Rf parameters for the CUPID photogun

Parameter	Value	Unit
Frequency	11.424	GHz
Q_l	215	-
Q_0	6585	-
Coupling coefficient (β)	29.63	-
S_{11}	-0.59	dB
Input peak power	166.5	MW
Field gradient at cathode	500	MV/m

accommodate the physical size of a solenoid designed for CUPID photoinjector. Design studies of the CUPID photogun were conducted using the commercial software Ansys HFSS and cross-checked with multiphysics software suite ACE3P [36, 37]. Visualizations for ACE3P were performed using Paraview [38].

Rf parameters are summarized at Tab. I. The frequency separation between π -mode at 11.424 GHz and the next nearest mode is 212 MHz, which is larger than the 100 MHz bandwidth of rf pulse compression network that is connected to the CUPID photogun. This means compressed pulses centered on 11.424 GHz will not excite the O-mode. Figure 5 shows the plot of simulated S_{11} reflection parameter of CUPID photogun. With a small S_{11} reflection parameter at -0.59 dB, more than 95 % of rf power will be reflected back from the CUPID photogun in the steady state. Hence, there are non-negligible fields present in the waveguide connecting the CUPID photogun and the TM_{01} mode launcher as shown in Fig. 4. This is a design choice to work with an existing mode launcher and alternatives will be investigated in the future. Fields present in the waveguide will have minimal impacts on the beam dynamics of emitted electrons, which will be discussed in Section III.

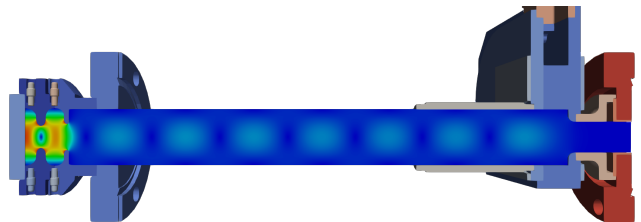


Figure 4. Cut-away view of the relative spacing between the CUPID photogun, the connecting waveguide, and the TM_{10} mode launcher, with superimposed π -mode field map. The relatively long waveguide connecting both components is a design choice to accommodate the physical size of a solenoid designed for CUPID photoinjector. Extended waveguide and solenoid are not shown in this view.

C. Time Domain Simulations

Time domain simulations of the CUPID photogun were performed to study its behavior in the short-pulse regime. This simulation is crucial as it allows us to study the build-up of fields and their field balance. Figure 6 shows the normalized experimental compressed pulse data used for our simulations, taken from [39]. The shaded area of Fig. 6 is the 20 ns region of interest that we used for time domain simulations. Figure 7 shows the time domain simulation of peak fields on the cathode (blue line) at 500 MV/m and the center of second cell (red line) at 490 MV/m with an input rf pulse (orange shaded area) at 166.5 MW peak power. Fields within the CUPID photogun reach their peak near steady-state in the time in-

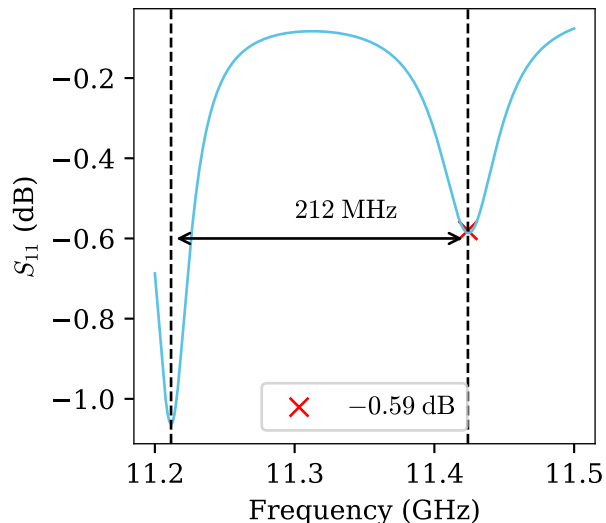


Figure 5. Plot of simulated S_{11} reflection parameter of the CUPID photogun. At 11.424 GHz, the S_{11} reflection parameter is -0.59 dB (“x” sign).

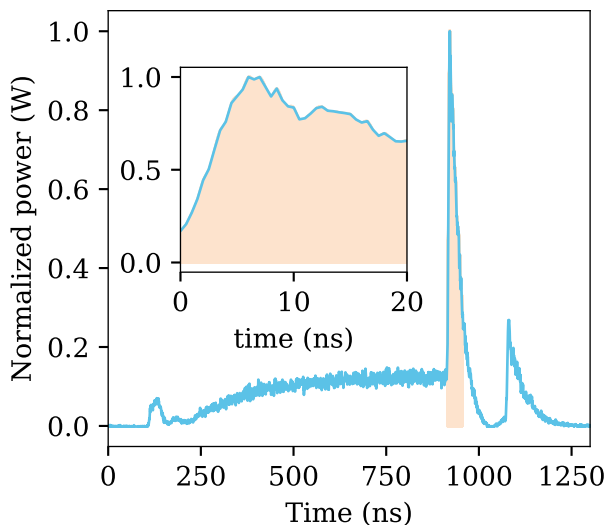


Figure 6. Plot of normalized power data from rf pulse compressors to be used for the CUPID photogun. The orange shaded region is the time period used for time domain simulations of CUPID photogun [39]

terval between 18 ns and 19 ns of the input pulse (inset of Fig. 7), indicating that this is the time window where photoemission should happen such that electrons are accelerated with the highest field gradient.

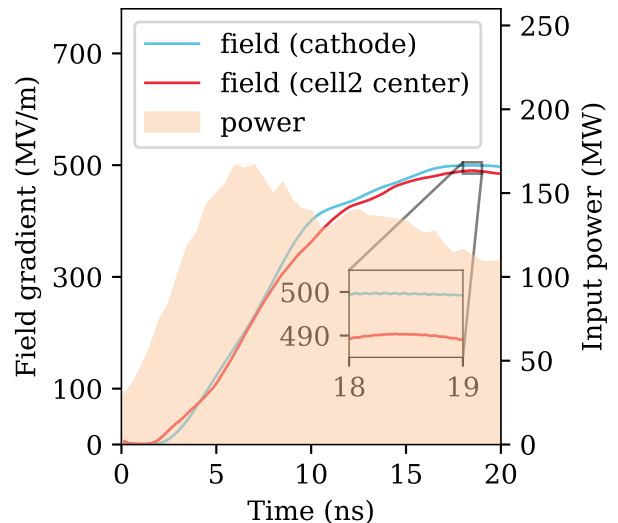


Figure 7. Plot of electric fields at the cathode (blue line) and the center of the second cell (red line) from time domain simulation of CUPID photogun with input power envelope (orange shaded area) at 166.5 MW peak power. The inset shows that the cathode reaches 500 MV/m peak field whereas the second cell reaches 490 MV/m peak field. Field balance to within 2% is achieved between both cells.

III. CUPID PHOTOINJECTOR BEAM DYNAMICS

A. CUPID Photoinjector

The CUPID photoinjector consists of the CUPID photogun, a superconducting solenoid and three downstream 1.2 m long 2.856 GHz accelerating structures.

1. CUPID Photogun

For an photogun operating in a steady-state regime, its on-axis field map $E_z(z, t)$ is described as

$$E_z(z, t) = \Re\{(E_{z,\text{real}}(z) + iE_{z,\text{imag}}(z))e^{i\omega t}\}, \quad (3)$$

where $E_{z,\text{real}}$ and $E_{z,\text{imag}}$ are the real and imaginary parts of an eigenmode solution of Maxwell equations, and $\Re\{\}$ is the operation of taking real part from the operand inside. We use this approach to approximate the on-axis field map of CUPID photogun for our subsequent beam dynamics studies using General Particle Tracer (GPT) simulation software [40], where the complex field maps were obtained from a snapshot in time of the time domain simulation shown in Fig. 7, at 18 ns where the field reaches quasi steady-state. We justify this approach by comparing it with time domain field maps taken from different snapshots in time. Figure 8 shows the comparison at different rf phases and both fields reach a good agreement.

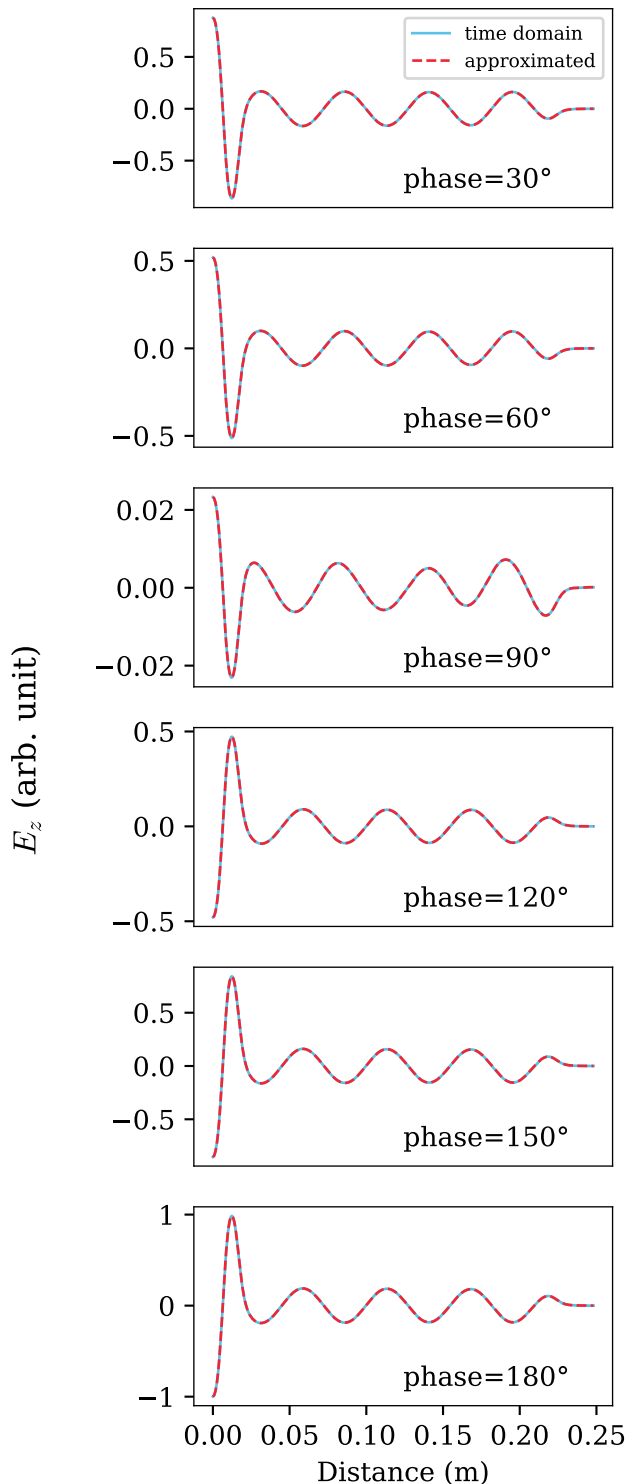


Figure 8. Plots of on-axis electric fields at different rf phases obtained using time domain simulations (blue lines) and Eq. 3 (red lines). Both fields reach a good agreement and hence justify the use of approximated electric field for beam dynamics simulations.

Figure 9 shows the beam energy (pink line) and time of arrival (blue line) at the exit of CUPID photogun (0.25 m from the cathode) with different rf phases, where the zero phase is defined as the phase where photoemission is first observed. The highest beam energy is 5.07 MeV with the on-crest launch phase at 76° and the time of arrival less than 0.9 ns. The evolution of the beam energy versus distance is shown in Fig. 10 (pink line) with the complex field magnitude (blue line) of CUPID photogun. Since CUPID photogun is designed to be over-coupled, there are non-negligible residual traveling waves present in the waveguide. As the phase of traveling waves is not adjusted to synchronize with the beam's phase, the beam experiences oscillation in its energy. Similar behavior was reported in ref.[29]. We made this design choice for having a long enough waveguide coupler to place a magnetic solenoid close to the CUPID photogun. Alternatives will be investigated in the future [28, 41].

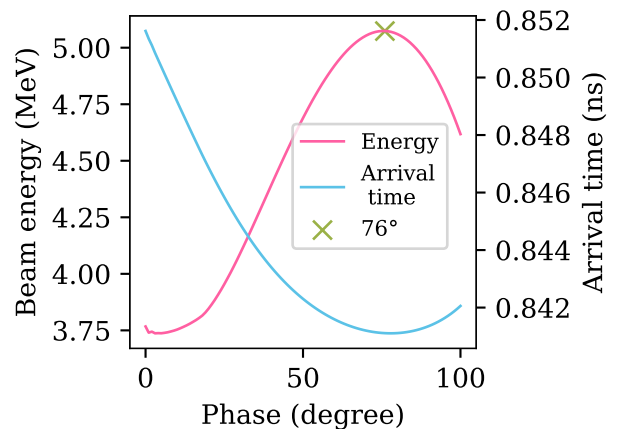


Figure 9. Plots of beam energy (pink line) and time of arrival (blue line) at the exit of CUPID photogun (0.25 m) from the cathode at different rf phases, where the zero phase is defined as the phase where photoemission is first observed. The highest beam energy is 5.07 MeV with the on-crest launch phase at 76° and the time of arrival less than 0.9 ns.

2. Solenoid

It is crucial to put a magnetic solenoid very close to an photogun to focus the photo-emitted electron beam. To provide a stable and high-strength magnetic field, we decided to use a superconducting solenoid for our CUPID photoinjector. It is envisioned that this superconducting solenoid will have a 0.09 m bore diameter, 0.4 m full length and provide up to 1 T peak magnetic field. A bucking coil will be employed to cancel the magnetic field at the center of the solenoid. Figure 11 shows the on-axis field profile of the superconducting solenoid, where the origin is the location of the cathode of CUPID photogun. Black dashed lines are the exits of the solenoid. The

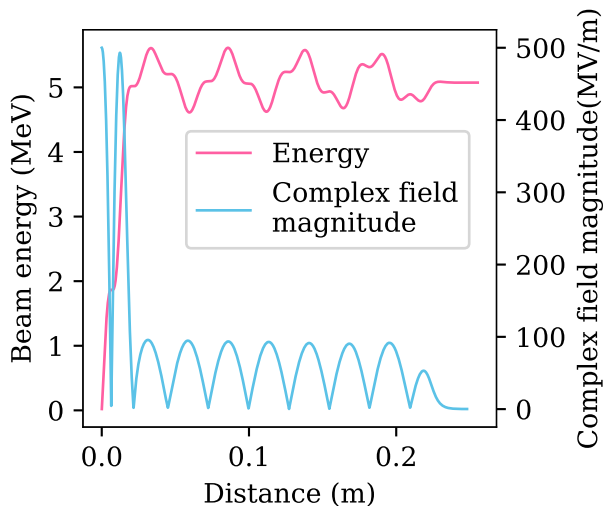


Figure 10. The evolution of the beam energy versus distance (pink line) with the complex field magnitude (blue line) of CUPID photogun. As the phase of traveling waves is not adjusted to synchronize with the beam’s phase, the beam experiences oscillation in its energy.

modeling and design of this superconducting solenoid was provided by Cryomagnetics, Inc [42].

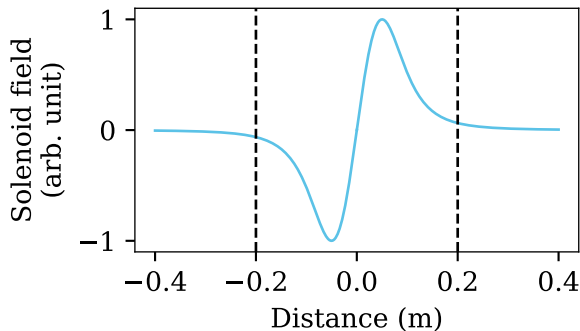


Figure 11. On-axis magnetic field profile of a superconducting solenoid used for the CUPID photoinjector, where the origin is the location of the cathode of the CUPID photogun. Black dashed lines are the exits of the solenoid. The modeling and design of this superconducting solenoid was provided by Cryomagnetics, Inc [42].

3. S-band Linacs

Three 1.2 m long S-band linacs operating at 2.856 GHz are used for our CUPID photoinjector. These linacs use the distributed-coupling design, with each structure having 20 accelerating cells to provide on-axis peak field at 100 MV/m [43]. Its on-axis field profile is shown in Fig. 12. These structures have an aperture radius of

14.12 mm, larger than that of the S-band linac in use at LCLS. This allows the structure to maintain beam emittance more easily. Due to the standing wave nature of the distributed coupling design, the accelerating fields are more stable as well.

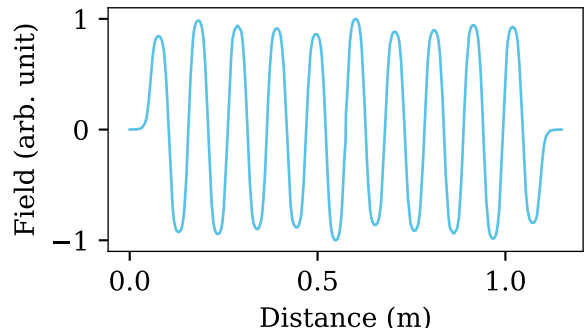


Figure 12. On-axis electric field of the 1.2 m long S-band linacs operating at 2.856 GHz are used for our CUPID photoinjector. Three such structures were used for beam dynamics simulations.

B. Beam Dynamics

We performed beam dynamics simulation studies of the CUPID photoinjector using GPT. Cylindrically-symmetric field maps were used for all accelerator components and three-dimensional mesh-based space-charge algorithm was used for 500 000 macroparticles in our simulations.

We were interested in the generation of high brightness beams at 100 pC total charge. The initial beam distribution had a mean transverse energy (MTE) of 400 meV, which corresponds to the thermal emittance of 0.9 $\mu\text{m}/\text{mm}$, given by

$$\frac{\varepsilon_n}{\sigma_x} = \sqrt{\frac{\text{MTE}}{mc^2}}, \quad (4)$$

where σ_x is the laser spot size [44]. The beam was assumed to have a uniform radial and flat top temporal distribution. We chose this value of MTE to match the measured MTE of the current LCLS photoinjector [45, 46].

We employed the emittance compensation scheme to achieve low emittance beams by focusing the beam to its beam waist to realign different longitudinal slices of the beam, followed by accelerating the beam to a very high energy to freeze the phase space oscillation of different longitudinal beam slices [14, 47, 48]. Figure 13 shows the evolution of electron beam’s transverse emittance (pink line) and its rms size (blue line) along the CUPID photoinjector. We achieved a 58 nm beam emittance using the CUPID photoinjector. Figure 14 shows the current profile (blue shaded area) and the beam’s

slice emittance (pink line). The beam core has 40 nm slice emittance and 28 A peak current. We note that CUPID photoinjector needs only one accelerating structure for emittance compensation, as shown in Fig. 12 where the beam’s emittance reaches a minimum near a distance of 2 m. Two additional structures were included in our studies to match the output beam energy of the current LCLS injector at 135 MeV [33]. We summarize our CUPID photoinjector and output beam parameters in Tab. II.

Note that our beam dynamics simulations did not take into account intrabeam scattering (IBS). IBS occurs due to short-range interactions between electrons, increasing the beam’s slice energy spread (SES) and degrading the six-dimensional brightness. IBS was studied in the past where it was concluded that the increase of IBS-induced SES was insufficient to affect the performance of x-ray FELs [49]. In addition, a laser heater was introduced to increase the SES to suppress the microbunching instability, such as in LCLS. Recent improvements in electron beam quality and SES measurement methods were able to confirm the effect of IBS in photoinjectors of modern FELs [50–53]. IBS-induced SES could be significant for the 100 pC low emittance beam that we were studying with CUPID, as reported in [54]. However, accurate simulation of IBS requires the calculation of one-to-one Coulomb interaction and thus requires a huge computational cost. Scaled-down simulations in ref [54] with similar beam parameters showed that IBS yielded less than 1 keV SES, which was still insufficient to affect the FEL performance that we are targeting. Experimental evidence of IBS-induced SES drove the theoretical and computational efforts in predicting IBS-induced SES, as reported in refs [55, 56]. On the other hand, IBS-induced SES can be used to suppress microbunching instability with some clever designs of accelerator lattice, as proposed in refs [50, 57, 58].

IV. LCLS WITH CUPID

With the low emittance beams obtained from CUPID photoinjector, we investigated the use of low emittance beams in the current LCLS copper accelerator to examine the potential performance improvement of the x-ray FEL. The LCLS copper accelerator consists of three linac sections L1, L2 and L3, an X-band harmonic linearizer section, two bunch compressors BC1 and BC2, a long transport beamline and a beam switchyard to deliver beams to the x-ray undulator beamline. Figure 15 shows the schematic diagram of the LCLS copper accelerator with the CUPID photoinjector.

At present, LCLS first accelerates and manipulates the electron beam’s longitudinal phase space at L1 and the X-band linearizer section, then it compresses the beam, followed by another acceleration and compression at L2 and BC2, further acceleration at L3, and finally delivers the beam through the transport line and beam switch-

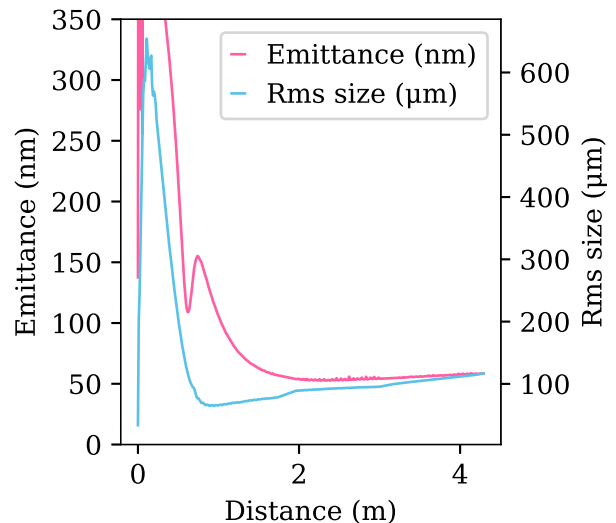


Figure 13. The evolution of beam’s emittance (pink line) and rms beam size (blue line) of CUPID photoinjector using parameters shown in Tab. II.

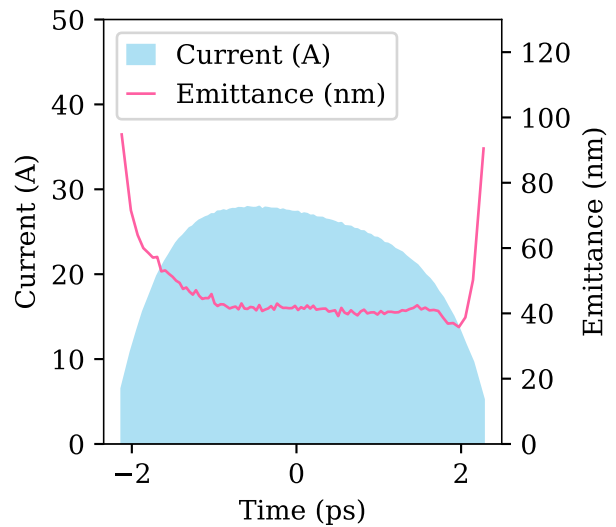


Figure 14. Current profile (blue shaded region) and slice emittance (pink line) of the beam at the end of CUPID photoinjector. The core emittance (at center) is 40 nm.

yard to the x-ray undulator beamline for coherent x-ray generation. The source of beam degradation in the LCLS copper accelerator includes wakefields in linac sections, coherent synchrotron radiation in bend sections (BC1, BC2 and beam switchyard), and longitudinal space charge throughout the whole accelerator. As the beam brightness is determined at its source, suppressing emittance growth is an important topic for a FEL.

In this section, we present our beam dynamics studies of LCLS with the CUPID photoinjector. In particular,

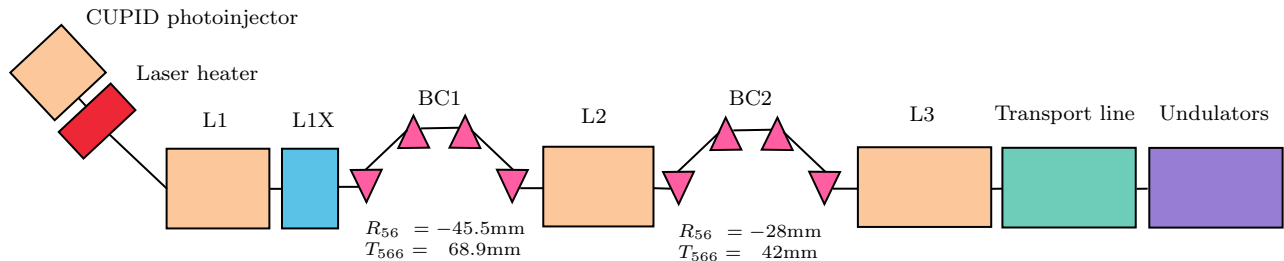


Figure 15. Schematic diagram of the LCLS copper accelerator with CUPID photoinjector and a laser heater. LCLS copper accelerator consists of three linac sections L1, L2 and L3, an X-band harmonic linearizer section L1X, two bunch compressors BC1 and BC2, a long transport beamline to deliver beams to the x-ray undulator beamline.

we were interested in the final beam parameter at the beginning of the x-ray undulator beamline for an energy range 14 GeV \sim 15 GeV for very hard x-ray generation and high pulse energy.

A. Simulation Setup for LCLS Copper Accelerator

The initial beam distribution used for LCLS beam dynamics studies was obtained from the output of the CUPID photoinjector in the previous section. We used the simulation software `elegant` version 2025.2 for our studies [59]. The output beam distribution file was converted from GPT format to an `elegant`-compatible format. In addition, we resampled the beam distribution using `elegant` script `smoothDist6s` to generate low-noise distribution to suppress numerical noise. We also trans-

formed the transverse phase space to fit the Twiss parameters of the LCLS copper accelerator entrance. Finally, we used a laser heater to increase the beam's SES by a few keV to suppress microbunching instability. It is noted that the effect of IBS could provide an increase in SES and thus eliminate the need of a dedicated laser heater. We reserve the topic of IBS and microbunching instability for our future studies.

B. LCLS Copper Accelerator Beam Dynamics with CUPID

Here we present LCLS beam dynamics simulation results using `elegant`. The longitudinal phase space (LPS) of the initial beam distribution is shown in Fig. 16 where the beam's SES was increased by 5 keV to suppress microbunching instability. The beam distribution was then transported through the whole LCLS copper accelerator using parameters shown in Tab. III. Figure 17 shows the LPS and the current profile respectively at (a)(d) the end of BC1, (b)(e) the end of BC2 and (c)(f) the entrance of undulator beamline. As the bending angles of bunch compressors BC1 and BC2 are fixed, we tuned linac phases to adjust compression factor. Rf phases of linac section L1 and X-band linearizer section L1X were adjusted to compress the beam to about 150 A peak current. A collimator in the mid section of BC1 were used to collimate the head and tail part of the beam to suppress current horns. The beam's total charge was reduced to 84 pC after passing through the collimator.

The beam was further accelerated through linac section L2 and compressed at BC2 to reach a peak current at 3000 A and 1600 A at the core of the beam, as shown in Fig. 17(b). The beam's slice emittances were increased after passing through BC2 as shown in Fig. 17(e), where the slice emittances of the both ends of beam were increased significantly compared to other beam slices. The beam reached final energy at 14.612 GeV at the entrance of undulator beamline as shown in Fig. 17(c). Slice emittances were increased significantly at both ends of beam but overall less than 100 nm as shown in Fig. 17(f). The beam core (at 0 fs) had 59 nm slice emittance and 0.005 % relative energy spread.

Table II. Optimized Parameters for the Injector and Final Beam Parameters

Parameter	Value	Unit
Laser spot size	66	μm
Laser duration	4.5	ps
Mean transverse energy	400	meV
Beam charge	100	pC
Gun frequency	11.424	GHz
Field on cathode	500	MV/m
Injection phase	71	$^\circ$
Linacs frequency	2.856	GHz
Linac 1 gradient	100	MV/m
Linac 1 phase (from on-crest)	6.4	$^\circ$
Linac 1 distance from the cathode	0.64	m
Linac 2 gradient	100	MV/m
Linac 2 phase (from on-crest)	0	$^\circ$
Linac 3 gradient	44	MV/m
Linac 3 phase (from on-crest)	0	$^\circ$
Solenoid field	0.62	T
Solenoid peak from the cathode	0.05	m
Final beam energy	135	MeV
Final beam bunch length	342	μm
Final beam rms size	62	μm
Final beam transverse emittance	58	nm
Final beam relative energy spread	0.09	%

We performed simulations with 250 pC nominal beam output from the existing LCLS injector and compare its results with the CUPID photoinjector. We hereby refer to this case as “LCLS nominal”. Accelerator parameters for LCLS nominal were similar to that of CUPID with minor changes in rf phases. Similarly, LCLS nominal beam was collimated at BC1 and reduced to 184 pC charge to suppress current horns. Figure 18 shows LPS and current profiles at the undulator entrance using (a)(c) CUPID photoinjector and (b)(d) LCLS nominal. LCLS nominal beam has a higher average current at 2000 A than CUPID beam at 1600 A but with much larger slice emittance at 430 nm (dashed line at (d)), whereas CUPID beam has overall less than 100 nm slice emittance (dashed line at (c)). Both have comparable slice energy spread.

Our results show a promising outcome with merely swapping the existing LCLS injector with CUPID photoinjector. Increases of the beam’s emittance were caused mainly by coherent synchrotron radiation effects at bunch compressors BC1, BC2 and the dispersive section of the long transport beamline. It is noted that the suppression of current horns on both ends of beam can be achieved using octupole magnets on both bunch compressors instead of collimating the beam [60]. Similarly, IBS-induced SES could be used instead of a laser heater to suppress microbunching instability [58]. In our studies, we chose to stick closely with the existing LCLS copper accelerator configuration to demonstrate the improvement of beam quality from the CUPID photoinjector. Additional upgrades and improvements to the LCLS copper accelerator complex would further enhance the benefits possible with a CUPID upgrade.

C. Simulation Setup for FEL

Beams from `elegant` simulations for both CUPID and LCLS nominal were transformed to match the Twiss pa-

Table III. Simulation Parameters for the LCLS copper accelerator and Final Beam Parameters

Parameter	Value	Unit
L1 phase (from on-crest)	-18	°
L1X phase (from on-crest)	-152.74	°
L2 phase (from on-crest)	-31.5	°
L3 phase (from on-crest)	0	°
BC1 R_{56}	-45.5	mm
BC1 T_{566}	68.9	mm
BC2 R_{56}	-28	mm
BC2 T_{566}	42	mm
Total charge (after collimator)	84	pC
Beam energy (initial)	135	MeV
Beam energy (after BC1)	223	MeV
Beam energy (after BC2)	5.106	GeV
Beam energy (undulator entrance)	14.612	GeV
Core emittance (undulator entrance)	59	nm
Core relative energy spread	0.005	%

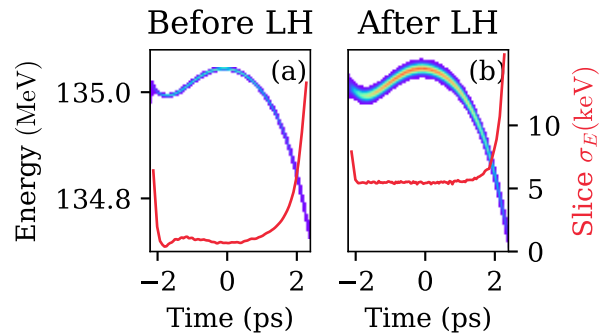


Figure 16. Longitudinal phase spaces of the beam (a) before laser heater and (b) after laser heater. Slice energy spread (red line) increases by 5 keV after the laser heater.

rameters of the entrance of LCLS hard x-ray undulator beamline. This undulator beamline is 150 m long, with undulator period $\lambda_u = 26$ mm and variable gap for adjustable undulator parameter K_u [61]. We used software `GENESIS1.3` [62] version 4.6.9 for our subsequent FEL simulations at photon energies 20, 30, 40, 50 and 60 keV to demonstrate performance improvement of x-ray generation from CUPID. Throughout our FEL simulations, undulator parameter K_u were adjusted to match the FEL resonance condition, using

$$\lambda_{\text{ph}} = \frac{\lambda_u}{2\gamma^2} \left(1 + \frac{K_u^2}{2} \right), \quad (5)$$

where λ_{ph} is the wavelength of x-ray photon, λ_u is the undulator period, γ is the beam’s Lorentz factor, K_u is the undulator parameter.

D. LCLS FEL Performance with CUPID

We summarize the FEL saturated pulse energy and power as functions of photon energy in Fig. 19 for CUPID (“×” sign in Fig. 19) and LCLS nominal (“+” sign in Fig. 19). In addition to `GENESIS1.3` simulations, we performed Ming-Xie parameterization analysis and its results (solid lines in Fig. 19) agree well with `GENESIS1.3` simulations. In general, CUPID performs better in all cases despite having lower total charge and average current. The FEL performance difference between CUPID and LCLS nominal becomes significant as photon energy goes higher. Total pulse energy of LCLS nominal for 40 keV photons drops to below 0.02 mJ, whereas CUPID maintains a pulse energy of 0.32 mJ. We show an example of FEL gain profiles at 40 keV for CUPID and LCLS nominal in Fig. 20. This is partly due to the fact that the present undulator beamline is shorter than the saturation length required for LCLS nominal to produce 40 keV photons, whereas CUPID reaches saturation after 50 m. In overall, CUPID maintains pulse energies over 0.1 mJ

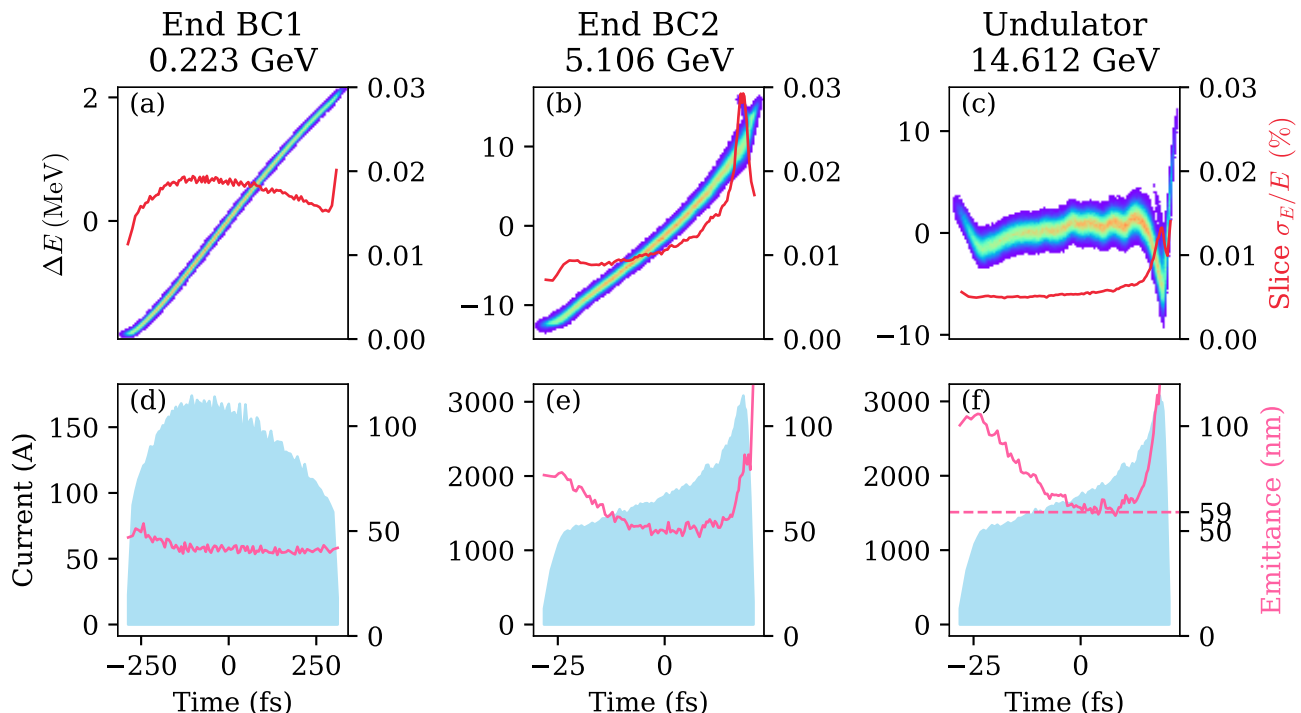


Figure 17. Longitudinal phase space and current profile respectively at (a)(d) the end of BC1, (b)(e) the end of BC2 and (c)(f) the entrance of undulator beamline. The beam was compressed and collimated at BC1 to remove current horns on both ends of the beam. It was further compressed at BC2 to reach 1600 A average current. The beam was further accelerated and transported to the entrance of undulator beamline at 14.612 GeV. Slice emittances were increased significantly but overall remained less than 100 nm.

for up to 60 keV photons before reaching the 150 m saturation length of the present LCLS undulator beamline. Ming Xie parameterization estimates that photon energy as high as 70 keV with a pulse energy of 0.01 mJ is achievable. In addition, it is noted that the present LCLS undulator beamline was designed for a photon energy range of 1 keV \sim 25 keV. Undulators tailored for very hard x-ray generation would further improve the FEL performance.

V. SUMMARY

We have presented CUPID, a high gradient photogun capable of delivering high brightness electron beams down to 58 nm transverse emittance at 100 pC. It is achieved by forming a photoinjector consists of the CUPID photogun, a dedicated superconducting solenoid, and downstream S-band accelerating structures. The CUPID photogun is designed to operate at 500 MV/m field at the cathode driven by high power nanosecond rf pulses. SLAC-built klystrons and recently commissioned rf pulse compressors are used to drive the CUPID photogun, instead of the wakefield acceleration approach of AWA, to benefit from klystron phase stability and arbitrary rf pulse shapes [63, 64].

Using the CUPID photoinjector for the existing LCLS

copper accelerator, our *elegant* simulations showed that final beam output for FEL is deliverable without modifications to the LCLS copper accelerator configuration with slice emittances of beam core below 100 nm. This is four times improvement over the LCLS nominal beam at 430 nm despite having lower average current. FEL simulations using GENESIS1.3 shows that CUPID beam delivers more than 0.1 mJ pulse energy up to 60 keV using the present hard x-ray undulator beamline of LCLS.

Experimental efforts on CUPID are ongoing where CUPID prototypes of different copper alloys were fabricated for rf testing. In parallel, rf pulse compressors and X-band klystrons were commissioned and have demonstrated more than 500 MW peak power, exceeding the requirements of the CUPID photogun. Near future plans include using rf pulse shaping for efficient peak power, and high power rf testing of CUPID photogun prototypes to investigate its feasibility. After that, the next step would be to commission the CUPID photogun in a dedicated accelerator test facility for electron beam generation. In addition, investigating the possibility of short pulse driven photogun at lower frequency bands would be an important topic for different accelerator applications. Investigating microscopic Coulomb interactions such as IBS would also be important.

CUPID represents a major step towards high gradi-

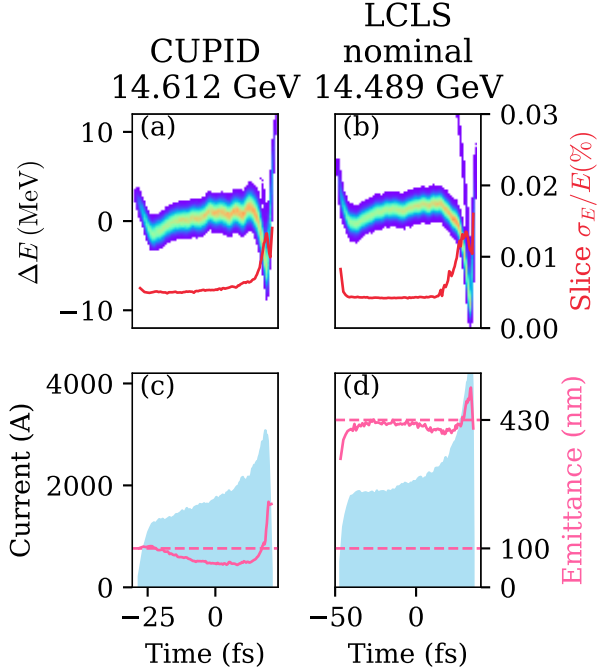


Figure 18. Comparison of longitudinal phase spaces using (a)(c) CUPID photoinjector and (b)(d) LCLS nominal injector. LCLS nominal beam has a higher average current at 2000 A than CUPID beam at 1600 A but with much larger slice emittance at 430 nm (dashed line at (d)), whereas CUPID beam has overall less than 100 nm slice emittance (dashed line at (c)). Both have comparable slice energy spread (red lines at (a)(b)).

ent photoguns through the use of short pulses driven by existing klystron technology. Our work here shows that performance improvement of LCLS FEL made possible through the use of the CUPID photogun. Newer accelerator technologies could be incorporated to achieve even better performance. Synergy between these topics and CUPID will be subjects for future studies.

ACKNOWLEDGMENTS

W.H.T thanks Zenghai Li, David Dowell, Valery Dolgashev, David Cesar and Emma Snively (SLAC), the Argonne Wakefield Accelerator group (ANL) for valuable discussions, R. Soliday (ANL), Ji Qiang (LBNL) and Andrea Latina (CERN) for help on simulations. This work is supported by the U.S. Department of Energy Contract No. DE-AC02-76SF00515 with SLAC National Ac-

celerator Laboratory. Simulation works used resources of the National Energy Research Scientific Computing (NERSC) Center and the SLAC Shared Science Data Facility (S3DF) at SLAC National Accelerator Laboratory. NERSC is a U.S. Department of Energy Office of Science User Facility located at Lawrence Berkeley Na-

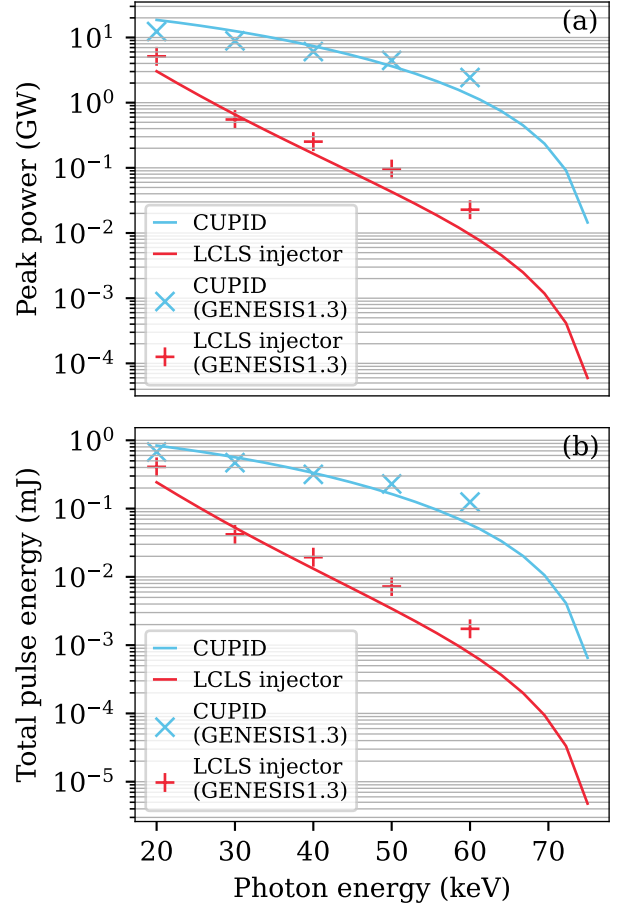


Figure 19. Comparison of hard x-ray FEL performance at different photon energies in terms of (a) peak power and (b) total pulse energy. Ming-Xie parameterization with beams from Fig. 18 were used. CUPID (blue line) outperforms LCLS nominal (red line) in both power and total pulse energy. GENESIS1.3 simulation results show a good agreement (“x” sign for CUPID and “+” sign for LCLS nominal). CUPID maintains more than 0.1 mJ pulse energy up to 60 keV photon energy.

tional Laboratory, operated under Contract No. DE-AC02-05CH11231.

[1] X. Wang, P. Musumeci, E. Lessner, and J. Goldstein, *Report of the Basic Energy Sciences Workshop on the*

Future of Electron Sources, September 8-9, 2016, Tech. Rep. (USDOE Office of Science (SC) (United States),

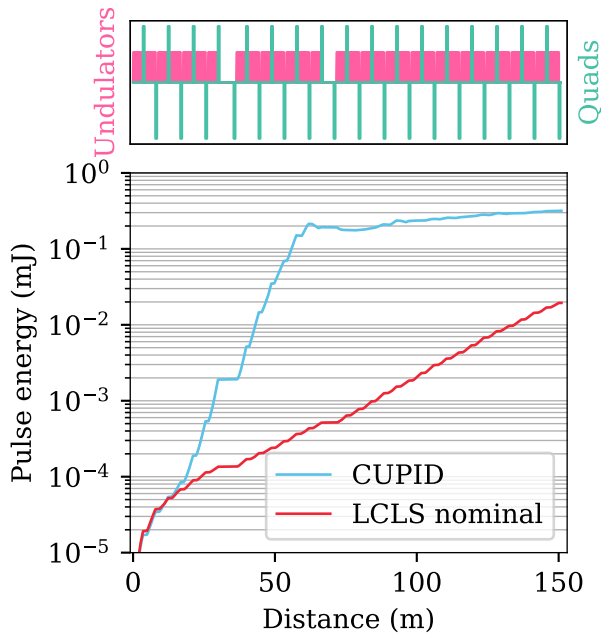


Figure 20. Comparison of total pulse energy for 40 keV x-ray photons using CUPID (blue line) and LCLS nominal (red line) with undulator beamline layout on top. The present undulator beamline is shorter than the saturation length required for LCLS nominal at 40 keV, whereas CUPID reaches saturation after 50 m.

- 2016).
- [2] P. Emma, R. Akre, J. Arthur, R. Bionta, C. Bostedt, J. Bozek, A. Brachmann, P. Bucksbaum, R. Coffee, F.-J. Decker, Y. Ding, D. Dowell, S. Edstrom, A. Fisher, J. Frisch, S. Gilevich, J. Hastings, G. Hays, P. Hering, Z. Huang, R. Iverson, H. Loos, M. Messerschmidt, A. Miahnahri, S. Moeller, H.-D. Nuhn, G. Pile, D. Ratner, J. Rzepiela, D. Schultz, T. Smith, P. Stefan, H. Tompkins, J. Turner, J. Welch, W. White, J. Wu, G. Yocky, and J. Galayda, First lasing and operation of an ångstrom-wavelength free-electron laser, *Nature Photonics* **4**, 641 (2010).
 - [3] C. Bostedt, S. Boutet, D. M. Fritz, Z. Huang, H. J. Lee, H. T. Lemke, A. Robert, W. F. Schlotter, J. J. Turner, and G. J. Williams, Linac coherent light source: The first five years, *Rev. Mod. Phys.* **88**, 015007 (2016).
 - [4] G. Crabtree, J. Sarrao, P. Alivisatos, W. Barletta, F. Bates, G. Brown, R. French, L. Greene, J. Hemminger, M. Kastner, *et al.*, *From Quanta to the Continuum: Opportunities for Mesoscale Science*, Tech. Rep. (USDOE Office of Science (SC) (United States), 2012).
 - [5] J. L. Barber, C. W. Barnes, R. L. Sandberg, and R. L. Sheffield, Diffractive imaging at large fresnel number: Challenge of dynamic mesoscale imaging with hard x rays, *Phys. Rev. B* **89**, 184105 (2014).
 - [6] R. Sheffield, C. Barnes, and J. Tapia, Matter-Radiation Interactions in Extremes (MaRIE) Project Overview, in *Proc. of International Free Electron Laser Conference (FEL'17), Santa Fe, NM, USA, August 20-25, 2017*, International Free Electron Laser Conference No. 38 (JACoW, Geneva, Switzerland, 2018) pp. 24–28, <https://doi.org/10.18429/JACoW-FEL2017-MOD06>.
 - [7] B. E. Carlsten, P. M. Anisimov, C. W. Barnes, Q. R. Marksteiner, R. R. Robles, and N. Yampolsky, High-brightness beam technology development for a future dynamic mesoscale materials science capability, *Instruments* **3**, 10.3390/instruments3040052 (2019).
 - [8] R. G. Kraus, D. Dattelbaum, and M. Knudson, *NNSA Light Source Enhancements: Coupling a High Energy Laser Driver to an XFEL*, Tech. Rep. (Lawrence Livermore National Laboratory (LLNL), Livermore, CA (United States), 2021).
 - [9] A. Benuzzi-Mounaix, F. Bertolotti, A.-C. Dippel, D. Dye, H. F. Poulsen, A. Madsen, M. M. Nielsen, S. Pascarelli, S. Pikuz, A. Rack, I. Robinson, K. Saksl, and U. Zastra, *Scientific Opportunities with very Hard XFEL Radiation*, Tech. Rep. REPORT. XFEL.EU WR-2024-002 (Schenefeld. 2024, 2024).
 - [10] J. B. Rosenzweig, N. Majernik, R. R. Robles, G. Andonian, O. Camacho, A. Fukasawa, A. Kogar, G. Lawler, J. Miao, P. Musumeci, B. Naranjo, Y. Sakai, R. Candler, B. Pound, C. Pellegrini, C. Emma, A. Halavanau, J. Hastings, Z. Li, M. Nasr, S. Tantawi, P. Anisimov, B. Carlsten, F. Krawczyk, E. Simakov, L. Failace, M. Ferrario, B. Spataro, S. Karkare, J. Maxson, Y. Ma, J. Wurtele, A. Murokh, A. Zholents, A. Cianchi, D. Cocco, and S. B. v. d. Geer, An ultra-compact x-ray free-electron laser, *New Journal of Physics* **22**, 093067 (2020).
 - [11] Z. Huang, M. Borland, P. Emma, J. Wu, C. Limborg, G. Stupakov, and J. Welch, Suppression of microbunching instability in the linac coherent light source, *Phys. Rev. ST Accel. Beams* **7**, 074401 (2004).
 - [12] M. Xie, Design optimization for an X-ray free electron laser driven by SLAC LINAC, *Conf. Proc. C* **950501**, 183 (1996).
 - [13] J. Fraser, R. Sheffield, and E. Gray, A new high-brightness electron injector for free electron lasers driven by RF linacs, *Nuclear Instruments and Methods in Physics Research Section A: Accelerators, Spectrometers, Detectors and Associated Equipment* **250**, 71 (1986).
 - [14] B. Carlsten, New photoelectric injector design for the los alamos national laboratory xuv fel accelerator, *Nuclear Instruments and Methods in Physics Research Section A: Accelerators, Spectrometers, Detectors and Associated Equipment* **285**, 313 (1989).
 - [15] K.-J. Kim, RF and space-charge effects in laser-driven RF electron guns, *Nuclear Instruments and Methods in Physics Research Section A: Accelerators, Spectrometers, Detectors and Associated Equipment* **275**, 201 (1989).
 - [16] J. Rosenzweig and E. Colby, Charge and wavelength scaling of RF photoinjector designs, *AIP Conference Proceedings* **335**, 724 (1995).
 - [17] I. V. Bazarov, B. M. Dunham, and C. K. Sinclair, Maximum achievable beam brightness from photoinjectors, *Phys. Rev. Lett.* **102**, 104801 (2009).
 - [18] D. Filippetto, P. Musumeci, M. Zolotarev, and G. Stupakov, Maximum current density and beam brightness achievable by laser-driven electron sources, *Phys. Rev. ST Accel. Beams* **17**, 024201 (2014).
 - [19] S. Döbert, R. Fandos, A. Grudiev, S. Heikkinen, J. A. Rodriguez, M. Taborelli, W. Wuensch, C. Adolphsen, and L. Laurent, High Power Test of an X-Band Slotted-iris Accelerator Structure at NLCTA, *Conf. Proc. C* **070625**,

- 2191 (2007).
- [20] F. Wang, Breakdown characteristics study on an 18 cell X-band structure, AIP Conference Proceedings **1086**, 373 (2009).
- [21] V. Dolgashev, S. Tantawi, Y. Higashi, and B. Spataro, Geometric dependence of radio-frequency breakdown in normal conducting accelerating structures, Appl. Phys. Lett. **97**, 171501 (2010).
- [22] L. Laurent, S. Tantawi, V. Dolgashev, C. Nantista, Y. Higashi, M. Aicheler, S. Heikkinen, and W. Wuensch, Experimental study of rf pulsed heating, Phys. Rev. ST Accel. Beams **14**, 041001 (2011).
- [23] A. Grudiev, S. Calatroni, and W. Wuensch, New local field quantity describing the high gradient limit of accelerating structures, Phys. Rev. ST Accel. Beams **12**, 102001 (2009).
- [24] C. Limborg-Deprey, C. Adolphsen, D. McCormick, M. Dunning, K. Jobe, H. Li, T. Raubenheimer, A. Vrieling, T. Vecchione, F. Wang, and S. Weathersby, Performance of a first generation x-band photoelectron RF gun, Phys. Rev. Accel. Beams **19**, 053401 (2016).
- [25] W. Graves, V. Bharadwaj, P. Borchard, V. Dolgashev, A. Goodrich, M. Holl, E. Nanni, and N. O'Brien, Design of an X-Band Photoinjector Operating at 1 kHz, in *8th International Particle Accelerator Conference* (2017).
- [26] R. A. Marsh, G. G. Anderson, S. G. Anderson, D. J. Gibson, C. P. J. Barty, and Y. Hwang, Performance of a second generation X-band RF photoinjector, Phys. Rev. Accel. Beams **21**, 073401 (2018).
- [27] J. Rosenzweig, A. Cahill, B. Carlsten, G. Castorina, M. Croia, C. Emma, A. Fukusawa, B. Spataro, D. Alesini, V. Dolgashev, M. Ferrario, G. Lawler, R. Li, C. Limborg, J. Maxson, P. Musumeci, R. Pompili, S. Tantawi, and O. Williams, Ultra-high brightness electron beams from very-high field cryogenic radiofrequency photocathode sources, 3rd European Advanced Accelerator Concepts workshop (EAAC2017) **909**, 224 (2018).
- [28] D. González-Iglesias, A. Aksoy, D. Esperante, B. Gimeno, A. Latina, M. Boronat, C. Blanch, N. Fuster-Martínez, P. Martínez-Reviriego, P. Martín-Luna, and J. Fuster, X-band RF photoinjector design for the CompactLight project, Nuclear Instruments and Methods in Physics Research Section A: Accelerators, Spectrometers, Detectors and Associated Equipment **1014**, 165709 (2021).
- [29] A. Giribono, D. Alesini, F. Cardelli, G. Di Raddo, L. Faillace, M. Ferrario, A. Gallo, A. Gizzi, S. Lauciani, A. Liedl, L. Pellegrino, L. Piersanti, C. Vaccarezza, A. Vannozzi, J. Scifo, L. Ficcadenti, G. Castorina, G. Pedrocchi, G. J. Silvi, and T. G. Lucas, Dynamics studies of high brightness electron beams in a normal conducting, high repetition rate C-band injector, Phys. Rev. Accel. Beams **26**, 083402 (2023).
- [30] W. H. Tan, S. Antipov, D. S. Doran, G. Ha, C. Jing, E. Knight, S. Kuzikov, W. Liu, X. Lu, P. Piot, J. G. Power, J. Shao, C. Whiteford, and E. E. Wisniewski, Demonstration of sub-GV/m accelerating field in a photoemission electron gun powered by nanosecond x-band radio-frequency pulses, Phys. Rev. Accel. Beams **25**, 083402 (2022).
- [31] M. Peng, J. Shao, C. Jing, E. C. Wisniewski, G. Ha, J. Seok, M. Conde, W. Liu, J. G. Power, D. Doran, C. Whiteford, and J. Shi, Generation of High Power Short Rf Pulses using an X-Band Metallic Power Extractor Driven by High Charge Multi-Bunch Train, in *10th International Particle Accelerator Conference* (2019) p. MOPRB069.
- [32] A. Dhar, M. Othman, and V. Dolgashev, Development of Ultra High Power Compact X-Band Pulse Compressor, in *16th Workshop on Breakdown Science and High Gradient Accelerator Technology* (2025).
- [33] R. Akre, D. Dowell, P. Emma, J. Frisch, S. Gilevich, G. Hays, P. Hering, R. Iverson, C. Limborg-Deprey, H. Loos, A. Miahnahri, J. Schmerge, J. Turner, J. Welch, W. White, and J. Wu, Commissioning the linac coherent light source injector, Phys. Rev. ST Accel. Beams **11**, 030703 (2008).
- [34] M. Dal Forno, *Design of a high power TM01 mode launcher optimized for manufacturing by milling*, Tech. Rep. (SLAC National Accelerator Lab., Menlo Park, CA (United States), 2016).
- [35] G. Torrisi, G. Sorbello, L. Celona, O. Leonardi, G. Mauro, S. Gammino, G. Castorina, B. Spataro, L. Faillace, and V. Dolgashev, Journal of Physics: Conference Series **1350**, 012188 (2019).
- [36] Ansys, Ansys High Frequency Structure Simulation (HFSS) Software, <https://www.ansys.com> (2025).
- [37] L. Xiao, L. Ge, Z. Li, and C.-K. Ng, Advances in multiphysics modeling for parallel finite-element code suite ACE3P, IEEE Journal on Multiscale and Multiphysics Computational Techniques **4**, 298 (2019).
- [38] J. Ahrens, B. Geveci, and C. Law, *ParaView: An End-User Tool for Large Data Visualization*, The visualization handbook, Vol. 717 (Elsevier, 2005).
- [39] A. Dhar, M. Othman, and V. Dolgashev, Development of ultra high power compact x-band pulse compressor, in *Proc. 16th International Particle Accelerator Conference, IPAC'25 - 16th International Particle Accelerator Conference No. 16* (JACoW Publishing, Geneva, Switzerland, 2025) pp. 1933–1936.
- [40] Pulsar Physics, General Particle Tracer (GPT), <https://www.pulsar.nl/gpt> (2025).
- [41] L. Faillace, R. Agustsson, M. Behtouei, F. Bosco, D. Bruhwiler, O. Camacho, M. Carillo, A. Fukasawa, I. Gadjev, A. Giribono, L. Giuliano, S. Kutsaev, N. Majernik, M. Migliorati, A. Mostacci, A. Murokh, L. Palumbo, B. Spataro, S. Tantawi, C. Vaccarezza, O. Williams, and J. Rosenzweig, High field hybrid photoinjector electron source for advanced light source applications, Physical Review Accelerators and Beams **25**, 063401 (2022), publisher: American Physical Society.
- [42] Cryomagnetics Inc, Cryomagnetics, Inc, <https://cryomagnetics.com> (2025).
- [43] A. Dhar, E. Nanni, G. White, M. Bai, M. Othman, S. Tantawi, and Z. Li, Distributed coupling linac for efficient acceleration of high charge electron bunches, JACoW **IPAC2024**, TUPR14 (2024).
- [44] D. H. Dowell and J. F. Schmerge, Quantum efficiency and thermal emittance of metal photocathodes, Phys. Rev. ST Accel. Beams **12**, 074201 (2009).
- [45] F. Ji, A Low Emittance Injector for LCLS-II HE (2022), Snowmass 2021 Electron Source Workshop.
- [46] T. Raubenheimer, X-ray FELs and LCLS-II (High Energy) (2022), UK Accelerator Institutes Seminar Series Autumn 2022.
- [47] L. Serafini and J. B. Rosenzweig, Envelope analysis of intense relativistic quasilaminar beams in rf photoinjectors: a theory of emittance compensation, Phys. Rev. E **55**, 7565 (1997).

- [48] M. Ferrario, J. E. Clendenin, D. T. Palmer, J. B. Rosenzweig, and L. Serafini, HOMDYN study for the LCLS RF photoinjector, in *2nd ICFA Advanced Accelerator Workshop on the Physics of High Brightness Beams* (2000) pp. 534–563.
- [49] Z. Huang, *Intrabeam scattering in an X-ray FEL driver*, Tech. Rep. SLAC-TN-05-026 (SLAC National Accelerator Laboratory, 2002).
- [50] S. Di Mitri, G. Perosa, A. Brynes, I. Setija, S. Spampinati, P. H. Williams, A. Wolski, E. Allaria, S. Brussaard, L. Giannessi, G. Penco, P. R. Rebernik, and M. Trovò, Experimental evidence of intrabeam scattering in a free-electron laser driver, *New Journal of Physics* **22**, 083053 (2020), publisher: IOP Publishing.
- [51] E. Prat, P. Dijkstal, E. Ferrari, A. Malyzhenkov, and S. Reiche, High-resolution dispersion-based measurement of the electron beam energy spread, *Phys. Rev. Accel. Beams* **23**, 090701 (2020).
- [52] E. Prat, P. Craievich, P. Dijkstal, S. Di Mitri, E. Ferrari, T. G. Lucas, A. Malyzhenkov, G. Perosa, S. Reiche, and T. Schietinger, Energy spread blowup by intrabeam scattering and microbunching at the swissfel injector, *Phys. Rev. Accel. Beams* **25**, 104401 (2022).
- [53] H. Qian, M. Krasilnikov, A. Lueangaramwong, X. Li, O. Lishilin, Z. Aboulbanine, G. Adhikari, N. Aftab, P. Boonpornprasert, G. Georgiev, J. Good, M. Gross, C. Koschitzki, R. Niemczyk, A. Oppelt, G. Shu, F. Stephan, G. Vashchenko, and T. Weilbach, Slice energy spread measurement in the low energy photoinjector, *Phys. Rev. Accel. Beams* **25**, 083401 (2022), publisher: American Physical Society.
- [54] R. R. Robles, O. Camacho, A. Fukasawa, N. Majernik, and J. B. Rosenzweig, Versatile, high brightness, cryogenic photoinjector electron source, *Physical Review Accelerators and Beams* **24**, 063401 (2021).
- [55] P. D. Valdor and others., Benchmarking intrabeam scattering with rf-track, in *Proc. 16th International Particle Accelerator Conference, IPAC'25 - 16th International Particle Accelerator Conference No. 16* (JACoW Publishing, Geneva, Switzerland, 2025) pp. 2333–2336.
- [56] T. G. Lucas, P. Craievich, E. Prat, S. Reiche, and E. Gjonaj, Accurate modelling of intrabeam scattering and its impact on photoinjectors for free-electron lasers (2025), arXiv:2510.02058 [physics.acc-ph].
- [57] S. Di Mitri and S. Spampinati, Estimate of free electron laser gain length in the presence of electron beam collective effects, *Phys. Rev. ST Accel. Beams* **17**, 110702 (2014).
- [58] J. Qiang, X-ray free electron laser linear accelerator without a laser heater, *Nuclear Instruments and Methods in Physics Research Section A: Accelerators, Spectrometers, Detectors and Associated Equipment* **1048**, 167968 (2023).
- [59] M. Borland, *elegant: A flexible SDDS-compliant code for accelerator simulation*, Technical Report LS-287 (Advanced Photon Source, Argonne National Laboratory, 2000).
- [60] N. Sudar, Y. Nosochkov, K. Bane, Z. Zhang, and Y. Ding, Octupole based current horn suppression in multistage bunch compression with emittance growth correction, *Physical Review Accelerators and Beams* **23**, 112802 (2020).
- [61] M. Leitner *et al.*, Hard X-Ray and Soft X-Ray Undulator Segments for the Linear Coherent Light Source Upgrade (LCLS-II) Project, in *Proc. of International Particle Accelerator Conference (IPAC'17), Copenhagen, Denmark, 14-19 May, 2017*, International Particle Accelerator Conference No. 8 (JACoW, Geneva, Switzerland, 2017) pp. 1605–1608, <https://doi.org/10.18429/JACoW-IPAC2017-TUPAB123>.
- [62] S. Reiche, GENESIS 1.3: a fully 3d time-dependent fel simulation code, *Nuclear Instruments and Methods in Physics Research Section A: Accelerators, Spectrometers, Detectors and Associated Equipment* **429**, 243 (1999).
- [63] C. Liu, A. Dhar, R. Herbst, and E. A. Nanni, High precision rf pulse shaping with direct rf sampling for future linear accelerators (2025), arXiv:2505.22872 [physics.acc-ph].
- [64] C. Liu, E. Snively, R. Herbst, K. Kim, and E. A. Nanni, Next generation direct rf sampling llrf control and monitoring system for linear accelerators (2025), arXiv:2509.09905 [physics.acc-ph].